OPTICS

Deep compressed multichannel adaptive optics scanning light ophthalmoscope

Jongwan Park[1], Kristen Hagan[1]†, Theodore B. DuBose[1]‡, Ramiro S. Maldonado[2], Ryan P. McNabb[2], Alfredo Dubra[3], Joseph A. Izatt[1,2]§, Sina Farsiu[1,2]*

Adaptive optics scanning light ophthalmoscopy (AOSLO) reveals individual retinal cells and their function, microvasculature, and micropathologies in vivo. As compared to the single-channel offset pinhole and two-channel split-detector nonconfocal AOSLO designs, by providing multidirectional imaging capabilities, a recent generation of multidetector and (multi-)offset aperture AOSLO modalities has been demonstrated to provide critical information about retinal microstructures. However, increasing detection channels requires expensive optical components and/or critically increases imaging time. To address this issue, we present an innovative combination of machine learning and optics as an integrated technology to compressively capture 12 nonconfocal channel AOSLO images simultaneously. Imaging of healthy participants and diseased subjects using the proposed deep compressed multichannel AOSLO showed enhanced visualization of rods, cones, and mural cells with over an order-of-magnitude improvement in imaging speed as compared to conventional offset aperture imaging. To facilitate the adaptation and integration with other in vivo microscopy systems, we made optical design, acquisition, and computational reconstruction codes open source.

INTRODUCTION

The utilization of adaptive optics (AO) technology in ophthalmic imaging has enabled in vivo visualization of retinal neurons and microvasculature (*1*–*4*) and has revolutionized our understanding of the structure, function, and neurophysiology of the visual system (*5*–*7*). Among AO-based imaging configurations, adaptive optics scanning light ophthalmoscopy (AOSLO) (*8*) is the most common system for in vivo visualization of individual retinal cells. High-resolution retinal images provided by AOSLO could be used for early diagnosis and prognosis of ophthalmic and neurological diseases (*9*–*12*). AOSLO-based biomarkers present a promising avenue to reduce the clinical trial duration for emerging therapies by providing objective, sensitive means to determine treatment efficacy (*13*–*16*). However, AOSLO can only be widely adopted in clinical practice if imaging can be done rapidly and accurately. Thus, developing fast AOSLOs is a prerequisite to using quantitative cellular-scale metrics as clinical end points.

In a point-scanning ophthalmoscope such as AOSLO, backscattered light emanating from each scan point can be divided into confocal and nonconfocal components. Confocal light, typically the central portion of reflected light 1 to 2 Airy disk diameters (ADD) in size, contains primarily singly scattered photons directly backscattered from the retina. Nonconfocal light, which refers to the light beyond this confocal region, is dominated by multiply scattered photons from various retinal layers, reflecting critical information about refractive index variations in thick retinal tissue (*17*, *18*). As the contrast of cellular features in an image is influenced by both the radial (*19*, *20*) and angular (*21*) positions of the detection channel, capturing the full two-dimensional (2D) distribution of multiply scattered light is crucial for obtaining comprehensive insights into retinal structure and function.

To date, capturing this 2D information has relied on two main methods, namely, multidetector (*19*, *22*) and (multi-)offset aperture (OA) (*2*, *20*, *21*) imaging, which have allowed for enhanced visualization of diverse retinal structures, including vessels (*21*, *22*), retinal ganglion cells (*2*, *20*), and immune cells (*20*, *23*). However, multidetector imaging requires an array of highly sensitive detectors, such as photomultiplier tubes (PMTs), which greatly increase system complexity and cost. OA imaging serially acquires individual nonconfocal channel images by moving a single detection channel, thus increasing the imaging duration at least linearly with the addition of each channel.

Here, we present an advanced imaging technique called deep compressed AOSLO (DCAOSLO) for rapid and cost-efficient nonconfocal light imaging by leveraging advances in compressed sensing (CS) and machine learning. Under mild conditions, CS can recover a high-dimensional signal from only a few linear random projections using a nonlinear reconstruction algorithm, surpassing the limit posed by the Nyquist-Shannon sampling theorem (*24*–*26*). On the basis of the single-pixel camera architecture (*27*–*32*) that can be easily incorporated into a typical AOSLO setup with minimal modification, in addition to the confocal channel, DCAOSLO efficiently samples 12 channels of nonconfocal light by making spatially multiplexed light measurements of selected channels using a digital micromirror device (DMD). Nonconfocal channel images are then simultaneously reconstructed using an unsupervised learning algorithm that does not require training data. Compared to the state-of-the-art OA imaging, we demonstrate the superior imaging performance of DCAOSLO with markedly increased acquisition speed in visualizing various healthy and diseased retinal microstructures.

RESULTS

DCAOSLO principle

DCAOSLO expedites the acquisition of nonconfocal channel images by compressively sampling light using a DMD. A DMD is a binary intensity spatial light modulator consisting of a regular array of small mirrors with two orientation states, *S1* and *S2*. If placed in a plane

[1]Department of Biomedical Engineering, Duke University, Durham, NC, USA. [2]Department of Ophthalmology, Duke University School of Medicine, Durham, NC, USA. [3]Byers Eye Institute, Stanford University, Stanford, CA, USA.
*Corresponding author. Email: sina.farsiu@duke.edu
†Present address: SpaceX, Redmond, WA, USA.
‡Present address: Apple Inc., Cupertino, CA, USA.
§Deceased.

conjugate to the retina in an AOSLO's detection arm, then the DMD can be programmed to display patterns that measure the nonconfocal light intensity of arbitrary aperture geometries. This DMD-based detection setup allows for a flexible nonconfocal channel configuration design, which can perform traditional OA imaging by displaying patterns where only one channel is active at a time and sequentially scanning over all channels. DCAOSLO improves this point sampling strategy using polymorphic patterns that scan all channels simultaneously (Fig. 1A).

At each scan point on the retina, nonconfocal light is coded by random (Bernoulli distribution, $P = 0.5$) patterns displayed on the DMD and then detected by two PMTs, PMT 1 and PMT 2, which

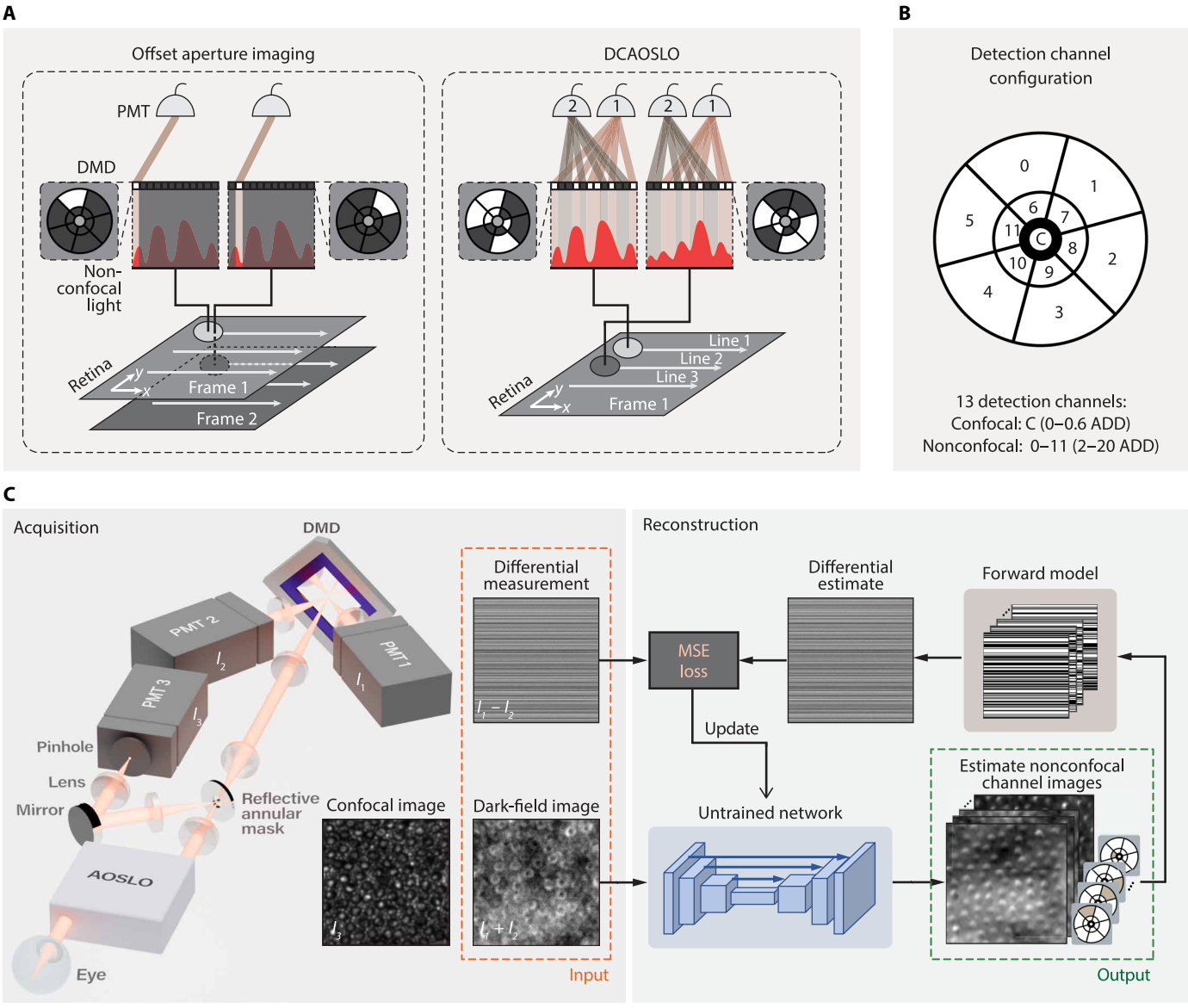

Fig. 1. DCAOSLO principle. (**A**) 1D representation of nonconfocal light sampling in OA and DCAOSLO imaging. OA imaging samples nonconfocal light one channel at a time. If implemented with a DMD, then this can be achieved by displaying patterns where only one channel is active during a raster scan and going through all channels by scanning the same retinal region multiple times. In DCAOSLO, multiple randomly selected channels of nonconfocal light are detected, and patterns are modulated at 15.3 kHz, the line rate of the horizontal resonant scanner. (**B**) Detection channel configuration used in this setup consisting of 1 confocal channel of size 0.6 ADD and 12 nonconfocal channels detecting the portion of light between 2 and 20 ADD. (**C**) Unified diagram of DCAOSLO acquisition and reconstruction. Acquisition: Reflective annular mask separates nonconfocal light from confocal light. PMT 1 and PMT 2 detect nonconfocal light coded by the DMD, while confocal light is detected by PMT 3. After raster scanning, a differential measurement is generated by subtracting PMT 2 image (I_2) from PMT 1 image (I_1) and the dark-field image via addition. Reconstruction: DCAOSLO uses an untrained deep generative CNN with randomly initialized weights as an indirect prior for image reconstruction. With the fixed input (dark-field image), the reconstruction network outputs estimate nonconfocal channel images. These estimate images are improved by iteratively refining the network by computing the mean squared error (MSE) loss between DCAOSLO's differential measurement and differential estimate generated by passing the estimated nonconfocal channel images through the DCAOSLO forward model.

detect summed light intensities from mirrors in *S1* and *S2* states, respectively (Fig. 1C). These patterns are refreshed at the line rate of AOSLO of 15.3 kHz, as determined by the resonant frequency of the horizontal resonant scanner. After 2D raster scanning, a differential measurement is obtained by subtracting the PMT 2 image from the PMT 1 image ($I_1 - I_2$), which removes the background and isotropically scattered light while retaining coded light information. Simultaneously, summing the PMT 1 and PMT 2 images ($I_1 + I_2$) provides a dark-field image where nonconfocal light is added and coding information is removed. Consequently, these DMD patterns constitute the mathematical forward model of DCAOSLO that describes how the differential measurement is generated from nonconfocal channel images we wish to recover.

Nonconfocal channel images are then simultaneously reconstructed using the deep image prior (DIP) (*33*) unsupervised learning technique, which uses an untrained, deep generative convolutional neural network (CNN) as an implicit image prior (Fig. 1C). During reconstruction, nonconfocal channel images are indirectly iteratively optimized as outputs of the generative reconstruction network by updating its randomly initialized weights. Optimal network weights are found by minimizing the mean squared error difference of DCAOSLO's differential measurement and the differential estimate obtained by passing the network outputs through the forward model. Instead of using the popular random noise as the network input for reconstruction, we used the dark-field image generated by summing PMT 1 and PMT 2 images, as it resulted in faster convergence by providing more image-specific information to the reconstruction network. DCAOSLO's mathematical and implementation details are provided in the Supplementary Text.

Microstamp photoreceptor phantom imaging

We first evaluated the performance of DCAOSLO (Fig. 2) by imaging a model eye consisting of an neutral density filter (Thorlabs), two 40-mm achromatic doublets (Thorlabs), and a photoreceptor phantom (Microstamp Research). The photoreceptor phantom was made up of polydimethylsiloxane 5-μm pillars in a hexagonal arrangement, mimicking the geometry of cone photoreceptor mosaic. The regular structure of this phantom gives rise to frequency peaks that correspond to two distinct spacings of pillars at $2d$ and $2d\sqrt{3}$,

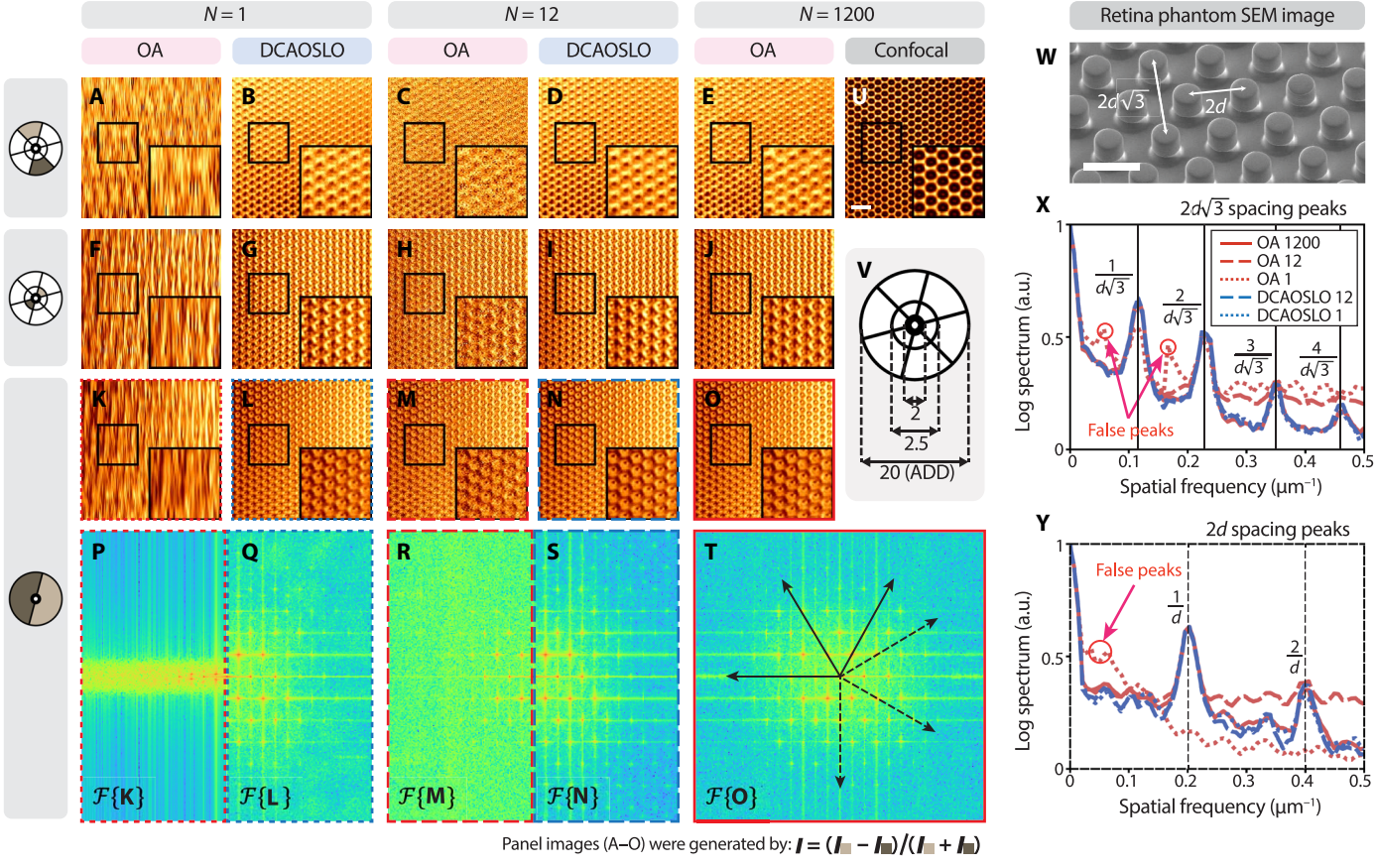

Fig. 2. Microstamp photoreceptor phantom imaging. (**A** to **O**) OA and DCAOSLO comparison of example differenced outer [(A) to (E)], differenced inner [(F) to (J)], and differenced summed nonconfocal channel images [(K) to (O)] of the photoreceptor phantom at full frame scans; $N = 1$, $N = 12$, and $N = 1200$. (**P** to **T**) Log-scale power spectra images by taking 2D fast Fourier transform of images in (K) to (O), respectively. (**U**) Averaged confocal image using 1200 frames ($N = 1200$). (**V**) Detection configuration used for phantom imaging. (**W**) A scanning electron microscope image of the phantom used in this experiment showing pillars in a hexagonal arrangement with two distinct pillar spacings of $2d\sqrt{3}$ and $2d$, where $d = 5$ μm. (**X** and **Y**) 1D-averaged spectrum comparison of OA and DCAOSLO with peaks that correspond to $2d\sqrt{3}$ (X) and $2d$ pillar spacings (Y) calculated by averaging 1D spectra along the directions of solid arrows and dashed arrows in (T), respectively. Red solid line (OA at $N = 1200$) is less visible due to close overlap with blue lines (DCAOSLO at $N = 1$ and 12). For better comparison, panel images (A) to (D) were histogram-matched to panel image (E), panel images (F) to (I) to panel image (J), and panel images (K) to (N) to panel image (O). SEM, scanning electron microscopy; a.u., arbitrary units. Scale bars, 25 μm (U) and 10 μm (W).

depending on the orientation at which the power spectrum is calculated on the Fourier-transformed image (Fig. 2W).

Figure 2 compares OA and DCAOSLO imaging by showing various representations of the 12 nonconfocal channel image sets that use different numbers of full frame scans (N). To acquire all 12 nonconfocal channel images, OA imaging requires at least 12 full frame scans, $N \geq 12$, over the same field of view (FOV). Faster imaging (scan rates at $N < 12$) can be achieved by sampling fewer horizontal lines, because resonant scanners allow subsampling in only one direction. Excessive line subsampling (e.g., at $N = 1$) leads to anisotropic aliasing (Fig. 2, A, F, and K), which cannot be recovered with interpolation and manifests as false peaks in the frequency domain (Fig. 2, X and Y). Moreover, OA images at the sampling rate of $N = 12$ (single frame per channel) are noisy (Fig. 2, C, H, and M), as evident in less distinctive frequency peaks at high harmonics (Fig. 2, X and Y), and require acquiring substantially more frames per channel for averaging. On the other hand, each DCAOSLO differential measurement encodes light intensity information of all channels, allowing for high-quality reconstructions of all nonconfocal channel images with just a single full frame scan (Fig. 2, B, G, and L). Comparable image qualities between DCAOSLO reconstructions with $N = 1$ and $N = 12$ scans and OA images generated by averaging 100 frames per channel at $N = 1200$ (Fig. 2, E, J, and O) are observed, further supported by the well-matching frequency peaks at all harmonics (Fig. 2, X and Y).

In vivo imaging of human subjects

A comparison between conventional OA and DCAOSLO's photoreceptor imaging of a healthy participant S1 without a history of ocular disease is shown in Fig. 3. To ensure a consistent retinal FOV across both nonconfocal imaging techniques, sequences of raw OA frames and DCAOSLO measurements were acquired, while the participant maintained fixation on a designated target. These sequences underwent eye motion correction using a modified version of the DeMotion strip-registration software (*34*) applied to simultaneously acquired confocal images. Subsequently, sets of N motion–corrected scans were selected for averaging (for OA) or reconstruction (for DCAOSLO). For OA imaging, at lower N levels, exactly N/12 frames were used for averaging per nonconfocal channel. At higher N levels, the numbers of frames varied slightly between channels due to the availability of registrable frames.

The cone and rod photoreceptors of healthy participants appear as bright spots in confocal images due to the photoreceptors' waveguiding properties (*35*). Nonconfocal images predominantly capture multiply scattered light from inner segments where cones present as side-illuminated spherical domes, with an illumination direction

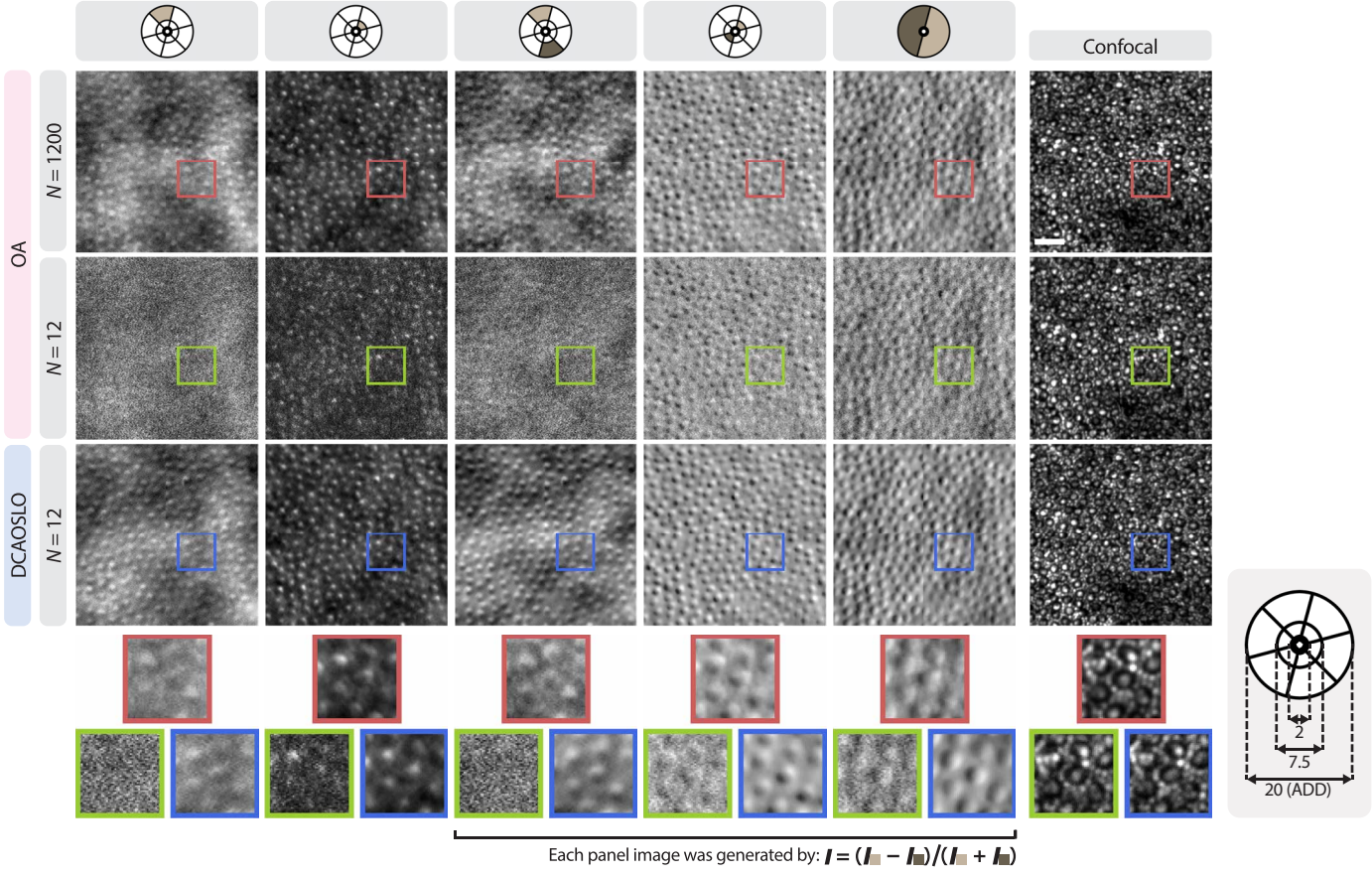

Fig. 3. In vivo photoreceptor imaging in the healthy participant S1. Comparison of OA and DCAOSLO outer, inner, differenced outer, differenced inner, and differenced summed nonconfocal channel images generated with different numbers of motion-corrected full frame scans (N). Panel images were histogram-matched column-wise, using the OA image at $N = 1200$ as the reference for each column. Scale bar, 25 μm. Confocal images capture intact cone and rod photoreceptors. Nonconfocal images capture cone inner segments that appear as side-illuminated spherical domes.

dependent on the angular position of the nonconfocal channel (*36*). However, a single OA frame per channel with $N = 12$ scans is noisy, making cone inner segments difficult to visualize on nonconfocal images even after enhancing contrast by differencing a pair of images from opposing channels. To address this limitation, we attempted to enhance individual OA channel images using DIP, a method proven effective for denoising tasks (*33*). As shown in the extended comparison of participant S1 in fig. S4, at $N = 12$, most cones remained indistinguishable in DIP-denoised images, which also introduced reconstruction artifacts. These structures were adequately visualized only by acquiring and averaging many of these noisy frames, thereby extending the imaging duration (e.g., averaging 100 frames per channel using $N = 1200$ scans).

In contrast, DCAOSLO allowed for clean reconstructions of underlying cones at $N = 12$, exhibiting image quality comparable to that achieved by OA at $N = 1200$. Notably, as shown in fig. S4, DCAOSLO generated high-quality reconstructions with as few as $N = 2$ frames, successfully visualizing cone inner segments across all channel images—a rate unattainable with OA imaging regardless of the sample's signal level. Comparison of all single nonconfocal channel images of S1 is shown in fig. S5. Additional healthy photoreceptor imaging in another participant S2 is provided in fig. S6.

To quantify image quality acquired with OA and DCAOSLO at different imaging rates, we evaluated the cone detection accuracy of a CNN-based automatic algorithm (Fig. 4) (*37*). This algorithm, trained on averaged, high-quality differenced nonconfocal cone images, served as an impartial metric for evaluating the quality of cone images acquired via OA and DCAOSLO imaging techniques. Compared to traditional image quality metrics such as peak signal-to-noise ratio (PSNR) and structural similarity index measure (SSIM), which require a near-perfect reference image, cone detection accuracy provides a more biologically meaningful measure of structural integrity in cone images (Supplementary Text and fig. S7). We examined the image quality of three types of differenced nonconfocal images—outer channel, inner channel, and the combination of all channels ("summed")—each exhibiting varying signal-to-noise ratio (SNR) but maintaining the orientation axis similar to that of the training data. The Dice's coefficient for each image was calculated on the basis of the ground truth cone locations, determined by manual correction of the automatically generated cone positions in the highest-quality differenced summed nonconfocal image of OA at $N = 1200$, along with its confocal image counterpart.

The bottom plot of Fig. 4 summarizes cone detection results from a cohort of three healthy volunteers, with data collected from

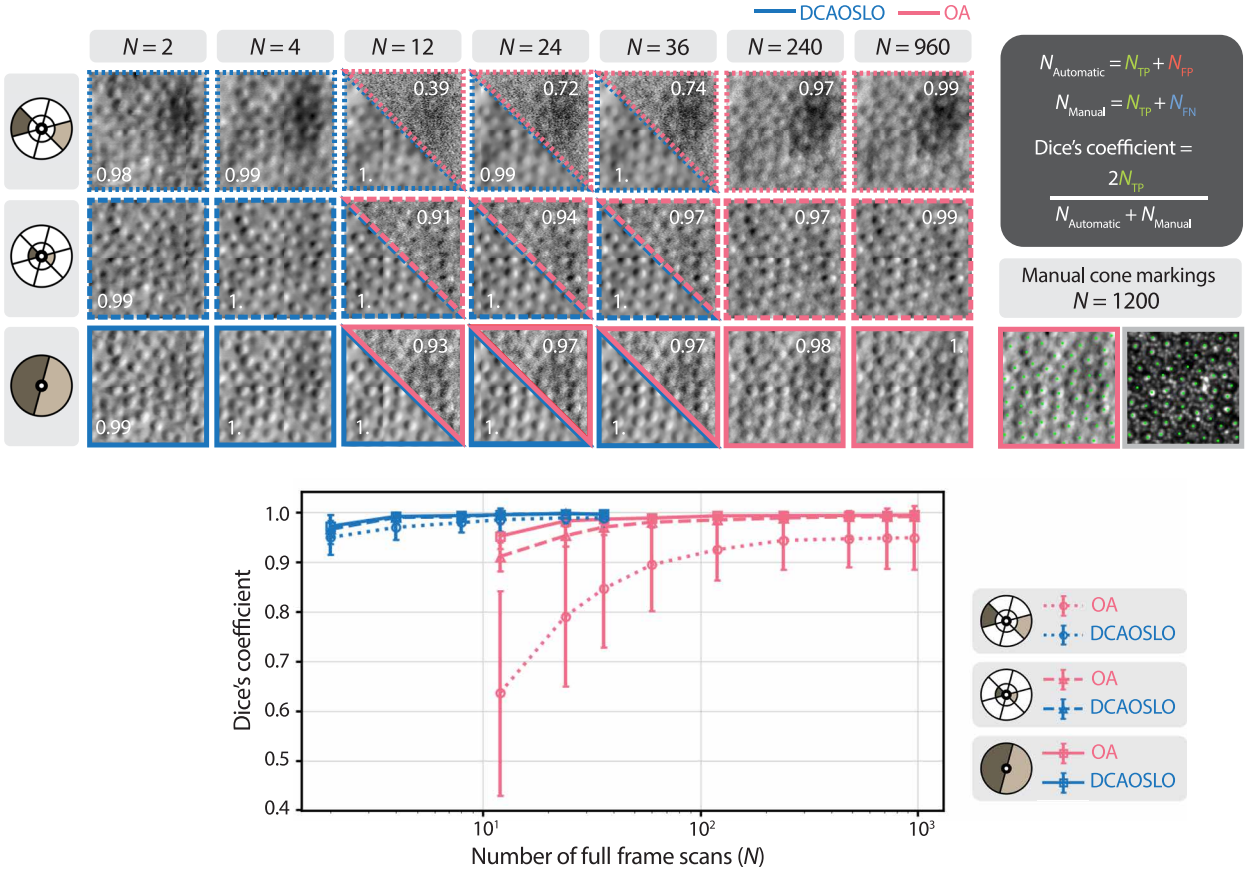

Fig. 4. Cone image quality analysis using an automatic cone detection algorithm (healthy participants). Quantitative image quality analysis of differenced outer, differenced inner, and differenced summed channel images based on automatic cone counting accuracy. Top image table shows example images from S1 used for analysis at various *N*, where the number in each image indicates the Dice's coefficient calculated by comparing the automatic cone identification on each image against the manual cone identification on $N = 1200$ images. Bottom plot compiles cone counting results over three healthy participants and two distinct retinal eccentricities each, by calculating the mean and SD of Dice's coefficients at each *N*.

two distinct retinal eccentricities for each individual. Across OA and DCAOSLO imaging techniques, consistent patterns emerged. Notably, cone detection accuracy increased as more full frame scans were used for reconstruction (in DCAOSLO) or averaging (in OA). Moreover, there was a gradual increase in cone detection accuracy in the order of differenced outer, differenced inner, and differenced summed nonconfocal images, reflecting their respective SNR differences. For differenced summed and differenced inner channel nonconfocal images with relatively higher SNR levels, DCAOSLO was able to achieve Dice's coefficients of 0.99 with as few as $N = 4$ scans, whereas OA required $N = 120$ and $N = 240$ scans, respectively, to attain a comparable level of accuracy. Similarly, in the case of differenced outer channel nonconfocal images, DCAOSLO achieved a Dice's coefficient of 0.95 with as few as $N = 2$ scans, in contrast to OA, which required $N = 480$ scans for a similar accuracy.

An extended comparison, which includes DIP-denoised OA images, is shown in fig. S8. For all image types—differenced outer (fig. S8A), differenced inner (fig. S8B), and differenced summed (fig. S8C)—DIP denoising provides some improvement in cone detection performance of OA images, particularly at lower N levels. However, its performance remains consistently below that of DCAOSLO and does not quite approach the accuracy levels achieved by DCAOSLO across the full range of N. Furthermore, the larger error bars observed in raw and DIP-denoised OA images highlight their inconsistent cone detection performance compared to DCAOSLO.

We also imaged patients with various ocular diseases. The comparison of OA and DCAOSLO imaging in a choroideremia patient S3 is shown in Fig. 5. In choroideremia, pathology can affect the morphology of cone photoreceptors, disrupting their waveguiding profiles. This results in irregular cone reflectivity in confocal AOSLO images, where cones can appear as either a low-contrast, dim spot or a cluster of bright spots that are indistinguishable from rods (*38*). Nonconfocal AOSLO imaging allows unambiguous identification of remnant cone inner segments, whose visualization can be expedited by DCAOSLO imaging.

At $N = 24$, OA captures two frames per channel, yet even after averaging, many cones remained unidentifiable due to noise. On the other hand, DCAOSLO consistently visualized cone inner segments throughout the FOV across all channels, including the detection of low-contrast cones in outer channel nonconfocal images that were not visible even after averaging approximately 78 OA frames per channel at $N = 937$. The superior imaging capabilities of DCAOSLO are further supported by the quantitative cone detection analysis from four subjects with various ocular diseases, as shown in Fig. 6. DCAOSLO was able to achieve Dice's coefficients of 0.89 for all image types with as few as $N = 12$ scans. In comparison, OA attained its peak Dice's coefficients of 0.85, 0.83, and 0.78 for differenced summed ($N = 480$), differenced inner channel ($N = 720$), and differenced outer channel images ($N = 720$), respectively. Extended comparison results for subject S3, demonstrating high-quality reconstructions with as few as $N = 4$ scans, are presented in fig. S9.

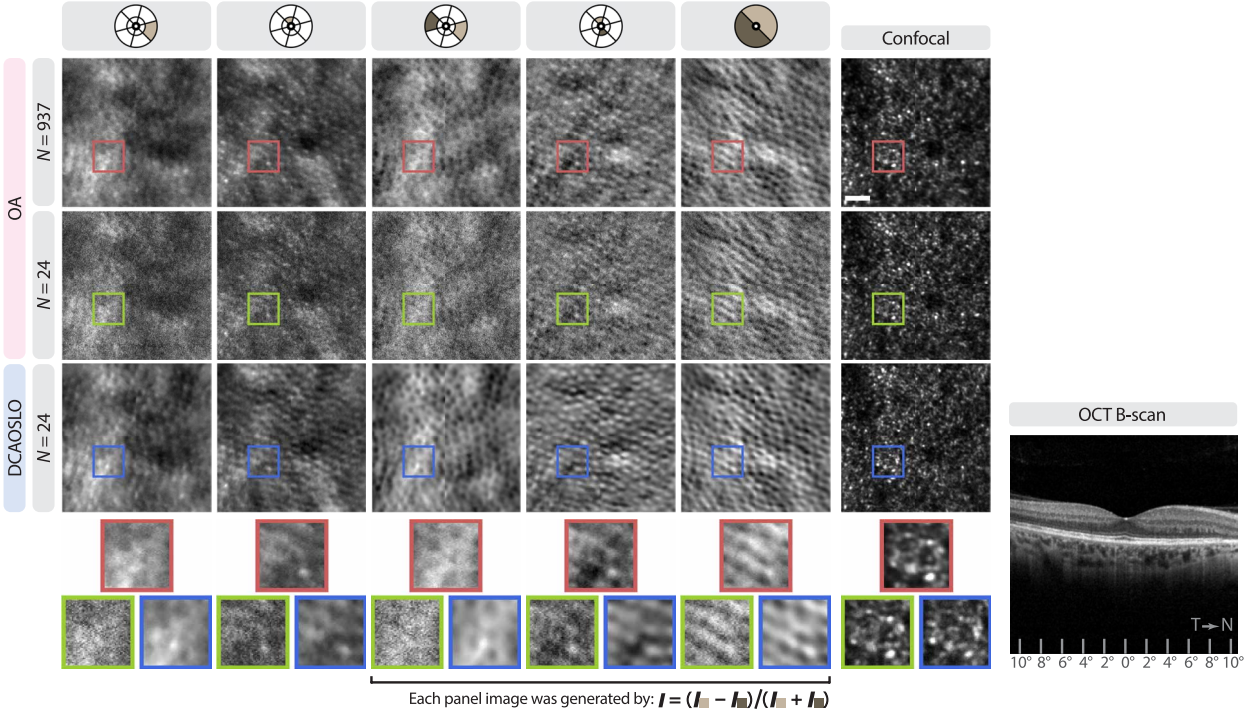

Fig. 5. In vivo photoreceptor imaging in the diseased subject S3 with choroideremia. Comparison of OA and DCAOSLO outer, inner, differenced outer, differenced inner, and differenced summed nonconfocal channel images, acquired at ~5° nasal (N). T, temporal. Panel images were histogram-matched column-wise, using the OA image at $N = 937$ as the reference for each column. Scale bar, 25 μm. Clinical optical coherence tomography (OCT) B-scan shows the abnormal ellipsoid zone band that terminates early at ~9°N due to pathology. Confocal images show dim, low-contrast cones with irregular reflectivity surrounded by rods. Nonconfocal images can better visualize remnant cone structures by capturing their inner segments.

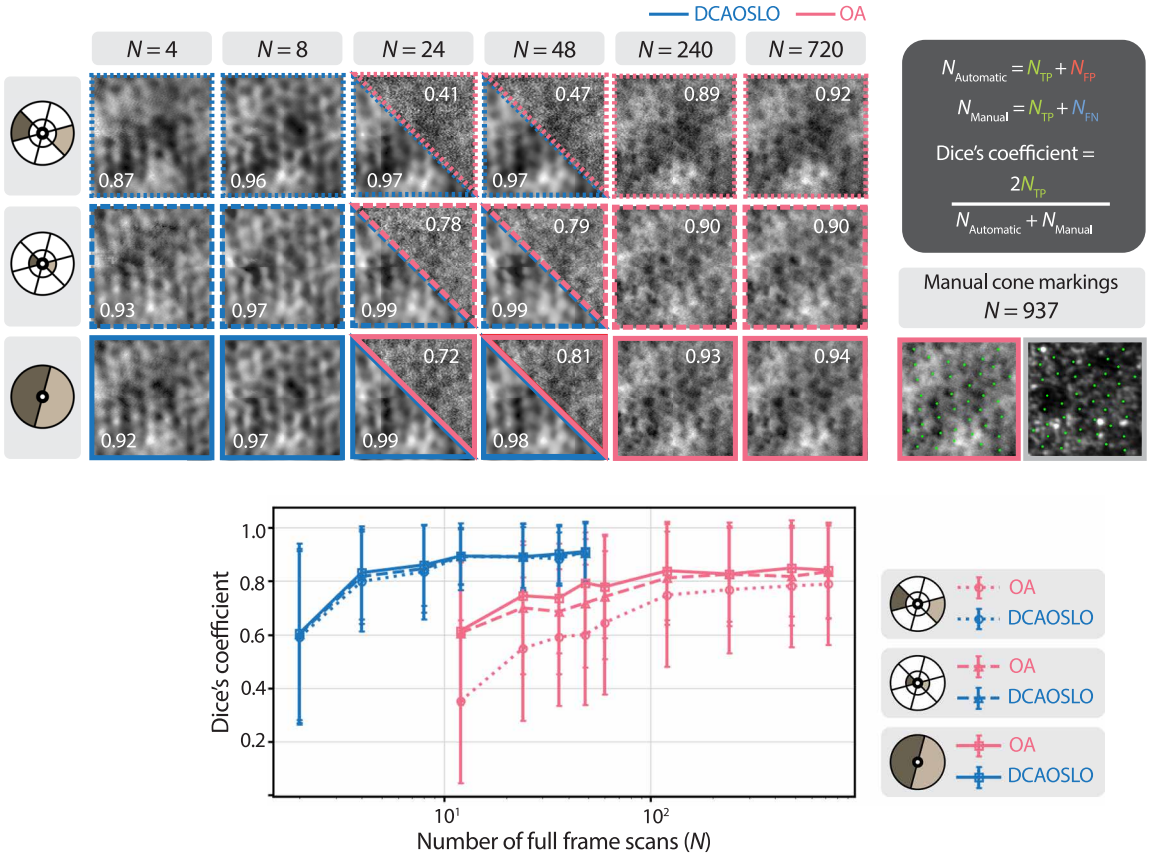

Fig. 6. Cone image quality analysis using an automatic cone detection algorithm (diseased subjects). Quantitative image quality analysis of differenced outer, differenced inner, and differenced summed channel images based on automatic cone counting accuracy. Top image table shows example images from S2 used for analysis at various *N*, where the number in each image indicates the Dice's coefficient calculated by comparing the automatic cone identification on each image against the manual cone identification on *N* = 937 images. Bottom plot compiles cone counting results over four subjects with various retinal diseases by calculating the mean and SD at each *N*.

Imaging results of an additional subject S4, with retinitis pigmentosa, are provided in fig. S10.

Beyond cone photoreceptors, nonconfocal AOSLO can improve the imaging of rod photoreceptors. Typically, in subjects with normal retinas, rods are not visualized by nonconfocal AOSLO due to limited resolution. However, in retinal diseases where rods may enlarge, nonconfocal AOSLO has demonstrated the capability of capturing rod inner segments (*36*, *39*). Figure 7 shows the comparison between OA and DCAOSLO's cone and rod photoreceptor imaging of subject S5 with Stargardt disease, where photoreceptors cannot be correctly identified solely on confocal images in the presence of extensive macular damage. However, nonconfocal images captured an irregularly shaped patch of remnant cones surrounded by rods. DCAOSLO enabled the visualization of individual rod inner segments with high fidelity using as few as $N = 12$ scans without the need for excessive averaging as in OA imaging. Extended comparison results for subject S5 using as few as $N = 2$ scans are presented in fig. S11. An additional photoreceptor imaging in patient S6 with Stargardt disease capturing both cone and rod inner segments is provided in fig. S12.

In nonconfocal channel images, the maximum contrast is generated along the angular orientation of the channel relative to the center of the detection plane. This anisotropic contrast mechanism directly affects the visualization of directional retinal structures, such as vessels, which can be entirely hidden if their orientation is orthogonal to that of the detection channel, as illustrated in fig. S13 (blue and red arrows). DCAOSLO's capability to generate contrast in multiple directions at high speeds renders it particularly effective for capturing these structures. The vessel imaging comparison between OA and DCAOSLO in a healthy participant S7 is shown in Fig. 8. While confocal images can effectively capture nerve fiber bundles and blood flow within large vessels, their strong backscattering signal can obscure the appearance of other important structures. Nonconfocal imaging can better visualize features, such as the microvasculature and larger vessel walls with their surrounding mural cells. Using just $N = 24$ scans, DCAOSLO was able to capture well-delineated vessel walls and surrounding mural cells, including pericytes (white arrowheads), and the smaller vessels branching out of the large vessel with high fidelity, matching OA images generated using $N = 948$ scans, whereas many of these structures remained unidentifiable in OA images generated using $N = 24$ scans. Extended comparison results for participant S7, demonstrating high-quality reconstructions with as few as $N = 2$ scans, are presented in fig. S14. An additional vessel imaging in a healthy participant S8 is shown in fig. S13.

DISCUSSION

Imaging speed is a critical consideration for eye examinations in clinics for light safety and patient comfort. In addition, AO imaging

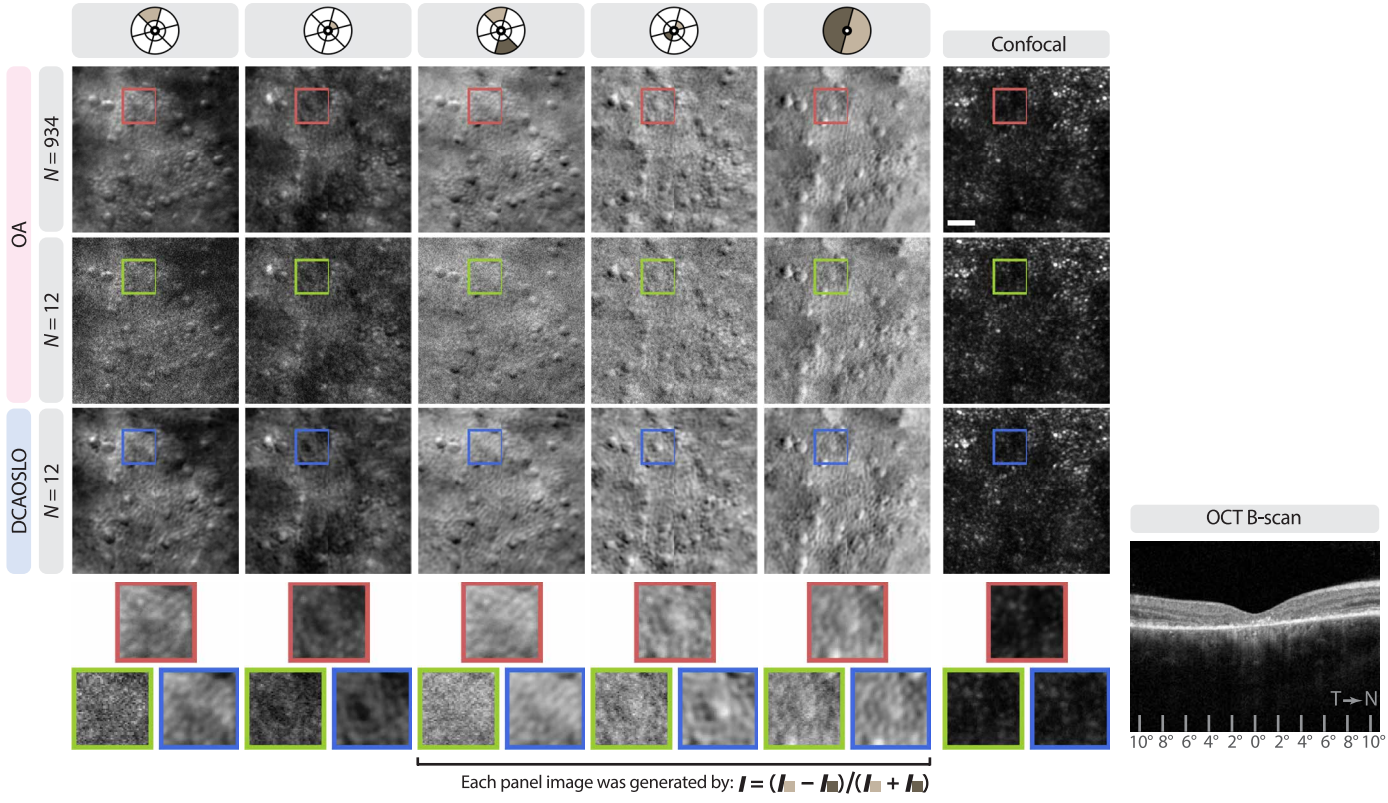

Fig. 7. In vivo photoreceptor imaging in the diseased subject S5 with Stargardt disease. Comparison of OA and DCAOSLO outer, inner, differenced outer, differenced inner, and differenced summed nonconfocal channel images, acquired at ~6°N. Panel images were histogram-matched column-wise, using the OA image at $N = 934$ as the reference for each column. Scale bar, 25 μm. Clinical OCT B-scan shows complete atrophy of the outer nuclear layer including absence of ellipsoid zone band in the central macula. It is hard to distinguish cones and rods from confocal images alone, which can be better visualized in nonconfocal images. Zoomed-in images show a cone inner segment surrounded by smaller rods.

systems often only achieve diffraction-limited imaging over small FOVs of ~1° across 6-mm pupil diameters and ~800-nm wavelengths, due to aberrations varying with retinal eccentricities (*40*–*42*). Because of this limitation, AOSLO requires the acquisition of images from multiple areas of the fundus to create a wide FOV image through tiling. DCAOSLO's rapid acquisition, with more than an order-of-magnitude improvement over OA, can facilitate high-resolution wide-field imaging of the fundus and capturing dynamic changes in the retina in a more diverse patient population, expediting the adoption of AOSLO imaging in the clinic.

Although two-channel split-detector (SD) imaging (*36*) cannot capture the comprehensive 2D distribution of nonconfocal light achieved by OA and DCAOSLO, it remains a popular nonconfocal imaging method due to its speed and light-efficient acquisition compared to OA. By leveraging patterns with varied split orientations and using both PMTs, DMD-based SD imaging enables rapid acquisition of nonconfocal images with multidirectional contrast. However, as detailed in fig. S15 and the corresponding discussion in Supplementary Text, by combining information from multiple channels, DCAOSLO can generate nonconfocal images with multidirectional contrast at an even faster rate than SD imaging. This enhanced capability establishes DCAOSLO as a more versatile, light-efficient, and cost-effective solution for advanced nonconfocal AOSLO imaging.

The DCAOSLO's CS technique has the potential to enhance the acquisition speed of any point-scanning microscopes that require multichannel light collection at each scan point, such as spectroscopy and image scanning microscopy (*43*, *44*). In microscopy, existing CS methods are primarily applied in wide-field imaging setups (*45*–*49*), which limit their use in confocal geometries—popular for imaging thick, highly scattering biological samples common in endoscopy or in vivo applications. Our proposed CS technique introduces simple add-on hardware based on a commercial DMD, which can be seamlessly integrated into typical scanning microscope setups, along with an unsupervised reconstruction method that is unbiased toward specific sample types. We further facilitate these adaptations by other teams by providing our open-source image acquisition, reconstruction code, and Zemax optical design along with this paper.

Further efforts are required to integrate the information derived from the cellular features visualized on individual nonconfocal channel images. While current techniques involving image filtering in either spatial frequency (*50*) or image domain (*23*) before image fusion have demonstrated improved cellular contrast, these methods are limited to using nonconfocal channels distributed at a fixed radial distance. The geometric optics model proposed by Guevara-Torres *et al.* (*17*) suggests that the 2D pattern of multiply scattered light at each scan point represents the phase shift of light caused by the translucent cell being illuminated, containing important information about the cell's 3D morphology and refractive index. This model implies the possible retrieval of quantitative phase information of the cell and their depth-resolved geometry through multichannel

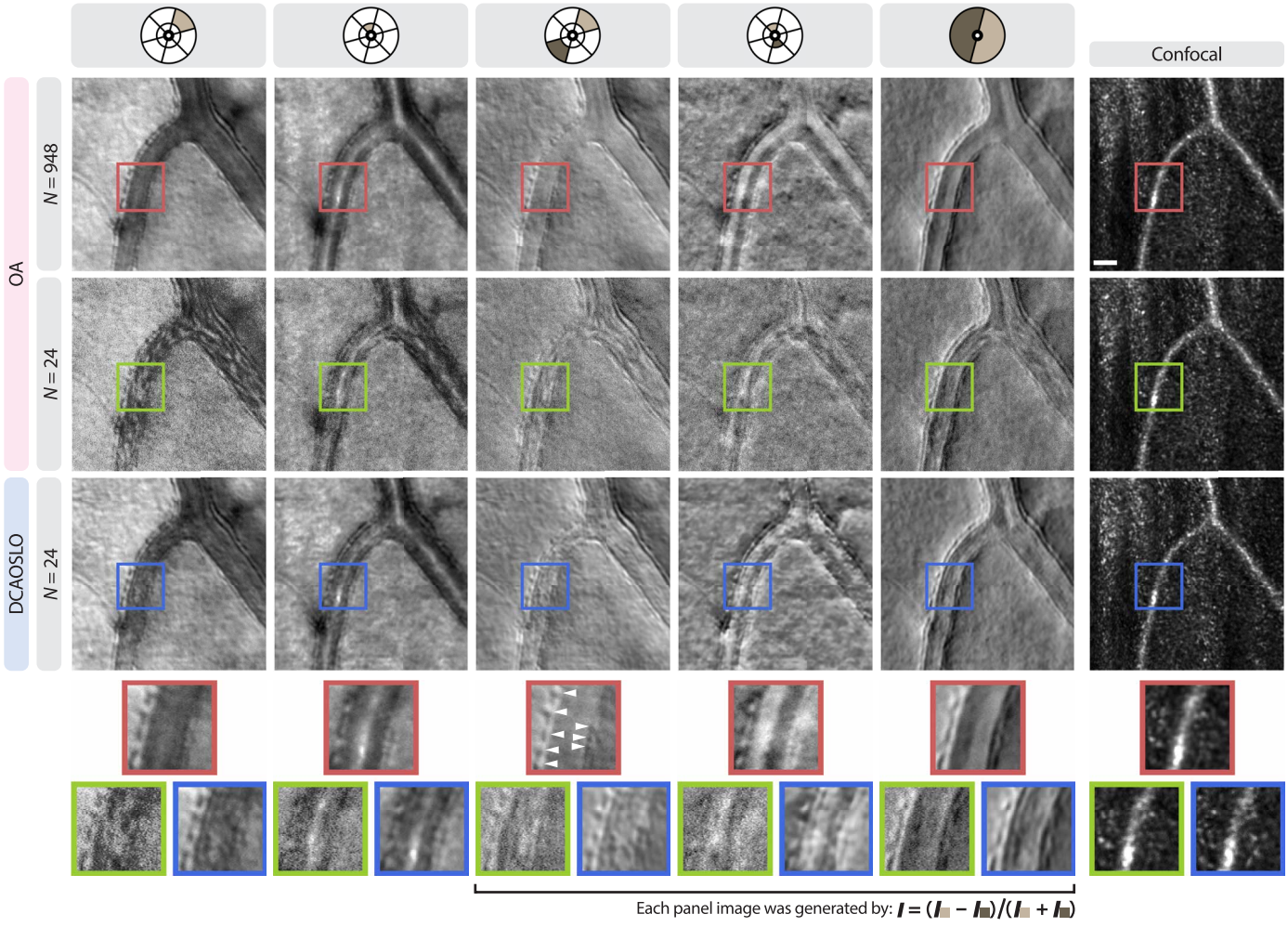

Fig. 8. In vivo retinal blood vessel imaging in the healthy participant S7. Comparison of OA and DCAOSLO outer, inner, differenced outer, differenced inner, and differenced summed nonconfocal channel images of a healthy participant S7. Panel images were histogram-matched column-wise, using the OA image at $N = 948$ as the reference for each column. Scale bar, 25 μm. Confocal images can effectively capture nerve fibers and bloodstream within large vessels. Compared to confocal imaging, nonconfocal images allow for visualization of detailed vessel wall structures, including endothelial cells and surrounding mural cells, e.g., pericytes (white arrowheads), as well as microvasculature.

nonconfocal AOSLO imaging, as shown in the preliminary work by Feng *et al.* (*51*). The integration of these image fusion techniques with DCAOSLO's rapid acquisition capabilities holds promise in maximizing the clinical utility of nonconfocal AOSLO imaging.

The current implementation of DCAOSLO is limited by the pattern refresh rate of the DMD. CS reconstruction relies on incoherence between samples. A higher pattern refresh rate can better capture the dynamic changes of nonconfocal light as the illumination spot raster scans the retina, leading to higher-quality reconstruction. We found that modulating patterns at the imaging raster line rate introduced strongly structured noise, appearing as horizontal line artifacts across the images. When channel images were reconstructed using popular plug-and-play algorithms (*52*, *53*), which integrate off-the-shelf denoisers such as total variation and block-matching and 4D filtering (BM4D) (*54*) as implicit regularizers, these artifacts remained prominent. In contrast, an untrained neural network exhibited an ability to resist fitting this structured noise with early stopping, producing cleaner and more accurate reconstructions, especially at low N levels (Supplementary Text and fig. S16). The proposed benchmark reconstruction method is suboptimal, and we expect that utilization of more recent image reconstruction methods, including latent diffusion models (*55*), will further improve the reconstruction performance.

In addition, DMD's light efficiency can suffer from various factors, including diffraction and array fill factor, resulting in an effective light efficiency of ~66% at 790 nm (*21*). Introducing an alternative spatial light modulation scheme, such as using a spinning mask coded with cyclic patterns capable of reaching switching rates in the megahertz range (*56*), could address this challenge. Nevertheless, DMD-based detection offers the advantage of a more flexible channel design, facilitating the optimization of the detection channel configuration, including channel geometry and resolution. In addition, our pattern switching strategy, synchronized with the horizontal resonant scanner running at 15.3 kHz, ensures stable coded light measurement without the need for a separate calibration step while maintaining the near-maximum pattern refresh rate achievable (Supplementary Text and fig. S3).

In summary, DCAOSLO is a rapid nonconfocal AOSLO imaging technique that compressively samples the 2D nonconfocal light intensity and reconstructs nonconfocal channel images using the state-of-the-art CNN-based algorithm that does not require training data. We have demonstrated DCAOSLO's superior imaging performance over conventional OA imaging with markedly faster acquisition speed in both healthy control participants and patients with ocular diseases in vivo. DCAOSLO's ability to provide fast and accurate visualization of various retinal cellular structures has the potential to cause a paradigm shift in the way ocular disease screening is performed, providing practical diagnostic tools and methodologies that could revolutionize the management of neurological and retinal diseases.

MATERIALS AND METHODS

Experimental design

All human experiments were conducted under a human imaging protocol approved by the Duke University Health System Institutional Review Board and adhered to the tenets of the Declaration of Helsinki. Written informed consent was obtained from all participants. Our study consisted of 13 healthy control participants without a history of ocular diseases of ages ranging from 21 to 34 and 16 subjects with various retinal diseases, such as autoimmune retinopathy, retinitis pigmentosa, Stargardt disease, and choroideremia, of ages ranging from 19 to 71. Data from some participants were excluded from analysis due to poor image quality, which prevented accurate cone counting, or insufficient data acquisition, resulting from difficulty maintaining fixation during imaging. Before imaging, all participants underwent pharmacological dilation via administration of a solution mix of 1% tropicamide and 2.5% phenylephrine. For each participant, an individualized dental putty teeth mold was made and combined with a bite bar for head stabilization.

A light-emitting diode array was used for external fixation to image various regions on the retina, which was also used to approximate the retinal eccentricities of collected images. For direct OA and DCAOSLO comparison, the identical fixation target was used to acquire images from the same retinal region between OA and DCAOSLO imaging, which were performed back-to-back by reconfiguring the acquisition and DMD control software. During in vivo imaging, we used real-time views of both confocal (I_3) and dark-field ($I_1 + I_2$) images in the acquisition software to guide the imaging process. In addition, SD imaging, simulated through DMD patterns, proved beneficial for optimizing the AO focus before performing OA and DCAOSLO imaging.

The measured powers of the 796-nm superluminescent diode (SLD) imaging source and 852-nm laser diode (LD) wavefront sensing beacon were ~470 and <50 μW at the subject cornea, respectively. Combined, these power levels were within the maximum permissible limit according to the American National Standards Institute Z136.1 (2022) power standard for continuous exposure (30,000 s) to a static point source.

DCAOSLO system design

The optical design schematic of DCAOSLO is shown in fig. S1. DCAOSLO was constructed by modifying the AOSLO design by Dubra and Sulai (*57*), which consisted of four concave spherical mirror telescopes arranged in a nonplanar folding configuration to minimize astigmatism. DCAOSLO used a 796-nm SLD (S-790-I-15-M, Superlum) as a point source for imaging and an 852-nm LD (LP852-SF30, Thorlabs) as a wavefront sensing beacon. With a horizontal resonant scanner running at 15.3 kHz, images were acquired at ~26 Hz over 1.2° square FOV. Ocular monochromatic aberrations were measured using a custom Shack-Hartmann wavefront sensor and corrected by a 97-actuator deformable mirror (ALPAO) at ~9 Hz.

The 796-nm collection arm of DCAOSLO incorporated a custom reflective elliptical annular mask positioned at ~50° in a descanned retinal conjugate plane to reflect the central circular 2 ADD of focal spot into the confocal detection arm and transmit 2 to 20 ADD into the nonconfocal detection arm. The 2 ADD confocal light was further filtered by a 0.6-ADD pinhole before reaching the PMT 3 for sub–Airy disk confocal detection. The 2- to 20-ADD nonconfocal portion of light was relayed onto a 1920-by-1080 DMD (DLP6500FYE, Texas Instruments) positioned in a second retinal conjugate plane. The DMD was rotated ~45° around the optical axis to keep the incoming and outgoing light in the same horizontal plane parallel to the optical table. Two PMTs, PMT 1 and PMT 2, were used to record the multiplexed light intensity from *S1* mirrors and *S2* mirrors, respectively. A lens was added before each PMT to collect diffracted light.

Supplementary Materials

This PDF file includes:

Supplementary Text
Figs. S1 to S16
Table S1
References

REFERENCES AND NOTES

1. Z. Liu, K. Kurokawa, F. Zhang, J. J. Lee, D. T. Miller, Imaging and quantifying ganglion cells and other transparent neurons in the living human retina. *Proc. Natl. Acad. Sci. U.S.A.* **114**, 12803–12808 (2017).
2. E. A. Rossi, C. E. Granger, R. Sharma, Q. Yang, K. Saito, C. Schwarz, S. Walters, K. Nozato, J. Zhang, T. Kawakami, W. Fischer, L. R. Latchney, J. J. Hunter, M. M. Chung, D. R. Williams, Imaging individual neurons in the retinal ganglion cell layer of the living eye. *Proc. Natl. Acad. Sci. U.S.A.* **114**, 586–591 (2017).
3. D. X. Hammer, A. Agrawal, R. Villanueva, O. Saeedi, Z. Liu, Label-free adaptive optics imaging of human retinal macrophage distribution and dynamics. *Proc. Natl. Acad. Sci. U.S.A.* **117**, 30661–30669 (2020).
4. T. Laforest, M. Künzi, L. Kowalczuk, D. Carpentras, F. Behar-Cohen, C. Moser, Transscleral optical phase imaging of the human retina. *Nat. Photonics* **14**, 439–445 (2020).
5. A. Roorda, D. R. Williams, The arrangement of the three cone classes in the living human eye. *Nature* **397**, 520–522 (1999).
6. L. C. Sincich, Y. Zhang, P. Tiruveedhula, J. C. Horton, A. Roorda, Resolving single cone inputs to visual receptive fields. *Nat. Neurosci.* **12**, 967–969 (2009).
7. E. A. Rossi, A. Roorda, The relationship between visual resolution and cone spacing in the human fovea. *Nat. Neurosci.* **13**, 156–157 (2010).
8. A. Roorda, F. Romero-Borja, W. J. Donnelly Iii, H. Queener, T. J. Hebert, M. C. W. Campbell, Adaptive optics scanning laser ophthalmoscopy. *Opt. Express* **10**, 405–412 (2002).
9. M. Paques, S. Meimon, F. Rossant, D. Rosenbaum, S. Mrejen, F. Sennlaub, K. Grieve, Adaptive optics ophthalmoscopy: Application to age-related macular degeneration and vascular diseases. *Prog. Retin. Eye Res.* **66**, 1–16 (2018).
10. N. Wynne, J. Carroll, J. L. Duncan, Promises and pitfalls of evaluating photoreceptor-based retinal disease with adaptive optics scanning light ophthalmoscopy (AOSLO). *Prog. Retin. Eye Res.* **83**, 100920 (2021).
11. A. Hargrave, N. Sredar, F. Khushzad, J. Yarp, A. Tomczak, M. Han, L. Kipp, A. Dubra, H. E. Moss, Novel foveal features associated with vision impairment in multiple sclerosis. *Invest. Ophthalmol. Vis. Sci.* **62**, 27–27 (2021).
12. G. McIlwaine, L. Csincsik, R. Coey, L. Wang, D. Fitzgerald, J. Moffat, A. M. Dubis, G. McDonnell, S. Hughes, T. Peto, I. Lengyel, Reduced cone density is associated with multiple sclerosis. *Ophthalmol. Sci.* **3**, 100308 (2023).
13. H. P. N. Scholl, R. W. Strauss, M. S. Singh, D. Dalkara, B. Roska, S. Picaud, J.-A. Sahel, Emerging therapies for inherited retinal degeneration. *Sci. Transl. Med.* **8**, 368rv6 (2016).
14. K. E. Talcott, K. Ratnam, S. M. Sundquist, A. S. Lucero, B. J. Lujan, W. Tao, T. C. Porco, A. Roorda, J. L. Duncan, Longitudinal study of cone photoreceptors during retinal

degeneration and in response to ciliary neurotrophic factor treatment. *Invest. Ophthalmol. Vis. Sci.* **52**, 2219–2226 (2011).
15. J. I. W. Morgan, Y. Y. Jiang, G. K. Vergilio, L. W. Serrano, D. J. Pearson, J. Bennett, A. M. Maguire, T. S. Aleman, Short-term assessment of subfoveal injection of adeno-associated virus-mediated *hCHM* gene augmentation in choroideremia using adaptive optics ophthalmoscopy. *JAMA Ophthalmol.* **140**, 411–420 (2022).
16. A. Pinhas, J. V. Migacz, D. B. Zhou, M. V. Castanos Toral, O. Otero-Marquez, S. Israel, V. Sun, P. N. Gillette, N. Sredar, A. Dubra, J. Glassberg, R. B. Rosen, T. Y. P. Chui, Insights into sickle cell disease through the retinal microvasculature: Adaptive optics scanning light ophthalmoscopy correlates of clinical OCT angiography. *Ophthalmol. Sci.* **2**, 100196 (2022).
17. A. Guevara-Torres, D. R. Williams, J. B. Schallek, Origin of cell contrast in offset aperture adaptive optics ophthalmoscopy. *Opt. Lett.* **45**, 840–843 (2020).
18. T. Y. P. Chui, D. A. VanNasdale, S. A. Burns, The use of forward scatter to improve retinal vascular imaging with an adaptive optics scanning laser ophthalmoscope. *Biomed. Opt. Express* **3**, 2537–2549 (2012).
19. N. Sredar, M. Razeen, B. Kowalski, J. Carroll, A. Dubra, Comparison of confocal and non-confocal split-detection cone photoreceptor imaging. *Biomed. Opt. Express* **12**, 737–755 (2021).
20. E. Gofas-Salas, Y. Rui, P. Mecê, M. Zhang, V. C. Snyder, K. V. Vienola, D. M. W. Lee, J.-A. Sahel, K. Grieve, E. A. Rossi, Design of a radial multi-offset detection pattern for in vivo phase contrast imaging of the inner retina in humans. *Biomed. Opt. Express* **13**, 117–132 (2022).
21. K. A. Sapoznik, T. Luo, A. De Castro, L. Sawides, R. L. Warner, S. A. Burns, Enhanced retinal vasculature imaging with a rapidly configurable aperture. *Biomed. Opt. Express* **9**, 1323–1333 (2018).
22. S. Mozaffari, V. Jaedicke, F. Larocca, P. Tiruveedhula, A. Roorda, Versatile multi-detector scheme for adaptive optics scanning laser ophthalmoscopy. *Biomed. Opt. Express* **9**, 5477–5488 (2018).
23. J. V. Migacz, O. Otero-Marquez, R. Zhou, K. Rickford, B. Murillo, D. B. Zhou, M. V. Castanos, N. Sredar, A. Dubra, R. B. Rosen, T. Y. P. Chui, Imaging of vitreous cortex hyalocyte dynamics using non-confocal quadrant-detection adaptive optics scanning light ophthalmoscopy in human subjects. *Biomed. Opt. Express* **13**, 1755–1773 (2022).
24. D. L. Donoho, Compressed sensing. *IEEE Trans. Inf. Theory* **52**, 1289–1306 (2006).
25. L. Gao, J. Liang, C. Li, L. V. Wang, Single-shot compressed ultrafast photography at one hundred billion frames per second. *Nature* **516**, 74–77 (2014).
26. B. Cleary, B. Simonton, J. Bezney, E. Murray, S. Alam, A. Sinha, E. Habibi, J. Marshall, E. S. Lander, F. Chen, A. Regev, Compressed sensing for highly efficient imaging transcriptomics. *Nat. Biotechnol.* **39**, 936–942 (2021).
27. M. P. Edgar, G. M. Gibson, M. J. Padgett, Principles and prospects for single-pixel imaging. *Nat. Photonics* **13**, 13–20 (2019).
28. B. Sun, M. P. Edgar, R. Bowman, L. E. Vittert, S. Welsh, A. Bowman, M. J. Padgett, 3D computational imaging with single-pixel detectors. *Science* **340**, 844–847 (2013).
29. C. M. Watts, D. Shrekenhamer, J. Montoya, G. Lipworth, J. Hunt, T. Sleasman, S. Krishna, D. R. Smith, W. J. Padilla, Terahertz compressive imaging with metamaterial spatial light modulators. *Nat. Photonics* **8**, 605–609 (2014).
30. Q. Pian, R. Yao, N. Sinsuebphon, X. Intes, Compressive hyperspectral time-resolved wide-field fluorescence lifetime imaging. *Nat. Photonics* **11**, 411–414 (2017).
31. S. Ota, R. Horisaki, Y. Kawamura, M. Ugawa, I. Sato, K. Hashimoto, R. Kamesawa, K. Setoyama, S. Yamaguchi, K. Fujiu, K. Waki, H. Noji, Ghost cytometry. *Science* **360**, 1246–1251 (2018).
32. D. Stellinga, D. B. Phillips, S. P. Mekhail, A. Selyem, S. Turtaev, T. Čižmár, M. J. Padgett, Time-of-flight 3D imaging through multimode optical fibers. *Science* **374**, 1395–1399 (2021).
33. D. Ulyanov, A. Vedaldi, V. Lempitsky, Deep image prior. *Int. J. Comp. Vis.* **128**, 1867–1888 (2020).
34. A. Dubra, Z. Harvey, in *Biomedical Image Registration*, B. Fischer, B. M. Dawant, C. Lorenz, Eds. (Springer, 2010), pp. 60–71.
35. D. T. Miller, D. R. Williams, G. M. Morris, J. Liang, Images of cone photoreceptors in the living human eye. *Vision Res.* **36**, 1067–1079 (1996).
36. D. Scoles, Y. N. Sulai, C. S. Langlo, G. A. Fishman, C. A. Curcio, J. Carroll, A. Dubra, In vivo imaging of human cone photoreceptor inner segments. *Invest. Opthalmol. Vis. Sci.* **55**, 4244–4251 (2014).
37. D. Cunefare, R. F. Cooper, B. Higgins, D. F. Katz, A. Dubra, J. Carroll, S. Farsiu, Automatic detection of cone photoreceptors in split detector adaptive optics scanning light ophthalmoscope images. *Biomed. Opt. Express* **7**, 2036–2050 (2016).
38. L. W. Sun, R. D. Johnson, V. Williams, P. Summerfelt, A. Dubra, D. V. Weinberg, K. E. Stepien, G. A. Fishman, J. Carroll, Multimodal imaging of photoreceptor structure in choroideremia. *PLOS ONE* **11**, e0167526 (2016).
39. M. M. Razeen, R. F. Cooper, C. S. Langlo, M. R. Goldberg, M. A. Wilk, D. P. Han, T. B. Connor Jr., G. A. Fishman, F. T. Collison, Y. N. Sulai, A. Dubra, J. Carroll, K. E. Stepien, Correlating photoreceptor mosaic structure to clinical findings in stargardt disease. *Transl. Vis. Sci. Technol.* **5**, 6 (2016).
40. D. R. Williams, P. Artal, R. Navarro, M. J. McMahon, D. H. Brainard, Off-axis optical quality and retinal sampling in the human eye. *Vision Res.* **36**, 1103–1114 (1996).
41. G. Smith, P. Bedggood, R. Ashman, M. Daaboul, A. Metha, Exploring ocular aberrations with a schematic human eye model. *Optom. Vis. Sci.* **85**, 330–340 (2008).
42. D. A. Atchison, D. H. Scott, Monochromatic aberrations of human eyes in the horizontal visual field. *J. Opt. Soc. Am. A* **19**, 2180–2184 (2002).
43. C. B. Müller, J. Enderlein, Image scanning microscopy. *Phys. Rev. Lett.* **104**, 198101 (2010).
44. M. Castello, G. Tortarolo, M. Buttafava, T. Deguchi, F. Villa, S. Koho, L. Pesce, M. Oneto, S. Pelicci, L. Lanzanó, P. Bianchini, C. J. R. Sheppard, A. Diaspro, A. Tosi, G. Vicidomini, A robust and versatile platform for image scanning microscopy enabling super-resolution FLIM. *Nat. Methods* **16**, 175–178 (2019).
45. V. Studer, J. Bobin, M. Chahid, H. S. Mousavi, E. Candes, M. Dahan, Compressive fluorescence microscopy for biological and hyperspectral imaging. *Proc. Natl. Acad. Sci. U.S.A.* **109**, E1679–E1687 (2012).
46. N. Radwell, K. J. Mitchell, G. M. Gibson, M. P. Edgar, R. Bowman, M. J. Padgett, Single-pixel infrared and visible microscope. *Optica* **1**, 285–289 (2014).
47. A. Escobet-Montalbán, R. Spesyvtsev, M. Chen, W. A. Saber, M. Andrews, C. S. Herrington, M. Mazilu, K. Dholakia, Wide-field multiphoton imaging through scattering media without correction. *Sci. Adv.* **4**, eaau1338 (2018).
48. D. Wu, J. Luo, G. Huang, Y. Feng, X. Feng, R. Zhang, Y. Shen, Z. Li, Imaging biological tissue with high-throughput single-pixel compressive holography. *Nat. Commun.* **12**, 4712 (2021).
49. Y. Liu, P. Yu, Y. Wu, J. Zhuang, Z. Wang, Y. Li, P. Lai, J. Liang, L. Gong, Optical single-pixel volumetric imaging by three-dimensional light-field illumination. *Proc. Natl. Acad. Sci. U.S.A.* **120**, e2304755120 (2023).
50. P. Mecê, E. Gofas-Salas, Y. Rui, M. Zhang, J.-A. Sahel, E. A. Rossi, Spatial-frequency-based image reconstruction to improve image contrast in multi-offset adaptive optics ophthalmoscopy. *Opt. Lett.* **46**, 1085–1088 (2021).
51. G. Feng, K. Kunala, Q. Yang, J. Schallek, *Quantitative Phase and Volumetric Retinal Imaging Using Angle-Resolved AOSLO Imaging* (SPIE BiOS, SPIE, 2023), vol. 12360.
52. S. V. Venkatakrishnan, C. A. Bouman, B. Wohlberg, in *2013 IEEE Global Conference on Signal and Information Processing* (IEEE, 2013), pp. 945–948.
53. U. S. Kamilov, H. Mansour, B. Wohlberg, A plug-and-play priors approach for solving nonlinear imaging inverse problems. *IEEE Signal Process. Lett.* **24**, 1872–1876 (2017).
54. M. Maggioni, V. Katkovnik, K. Egiazarian, A. Foi, Nonlocal transform-domain filter for volumetric data denoising and reconstruction. *IEEE Trans. Image Process.* **22**, 119–133 (2013).
55. R. Rombach, A. Blattmann, D. Lorenz, P. Esser, B. Ommer, in *Proceedings of the IEEE/CVF Conference on Computer Vision and Pattern Recognition* (IEEE, 2022), pp. 10684–10695.
56. E. Hahamovich, S. Monin, Y. Hazan, A. Rosenthal, Single pixel imaging at megahertz switching rates via cyclic Hadamard masks. *Nat. Commun.* **12**, 4516 (2021).
57. A. Dubra, Y. Sulai, Reflective afocal broadband adaptive optics scanning ophthalmoscope. *Biomed. Opt. Express* **2**, 1757–1768 (2011).
58. D. P. Kingma, J. Ba, paper presented at the International Conference on Learning Representations (ICLR), San Diega, CA, USA, 2015.
59. O. Ronneberger, P. Fischer, T. Brox, paper presented at the Medical Image Computing and Computer-Assisted Intervention–MICCAI 2015, Cham, 2015.

Acknowledgments: We thank A. Kuo for help in recruiting patients in the earlier stages of this project and for dilating normal subjects' eyes and C. Toth for help in attaining IRB. **Funding:** This work was supported by National Science Foundation grant CBET-1902904 (J.A.I. and S.F.), National Institutes of Health grant P30EY005722 (S.F.), National Institutes of Health grant P30EY026877 (A.D.), National Institutes of Health grant R01EY031360 (A.D.), National Institutes of Health grant R01EY032147 (A.D.), National Institutes of Health grant R01EY032669 (A.D.), Research to Prevent Blindness grants (S.F. and A.D.), and Foundation Fighting Blindness grant PPA-1224-0890-DUKE (S.F.). **Author contributions:** Conceptualization: T.B.D., J.A.I., and S.F. Methodology: J.P., K.H., R.P.M., A.D., J.A.I., and S.F. Investigation: J.P. Formal analysis: J.P., K.H., T.B.D., R.S.M., R.P.M., A.D., J.A.I., and S.F. Visualization: J.P. Supervision: J.A.I. and S.F. Writing—original draft: J.P. Writing—review and editing: J.P., K.H., T.B.D., R.S.M., R.P.M., A.D., J.A.I., and S.F. **Competing interests:** J.P., T.B.D., K.H., R.P.M., J.A.I., and S.F. are inventors on a patent application (US patent no. 2024/0423468 A1, published 26 December 2024) assigned to Duke University that covers this work on DCAOSLO. All other authors declare that they have no competing interests. **Data and materials availability:** All data needed to evaluate the conclusions in the paper are present in the paper and/or the Supplementary Materials. The datasets used in our paper, codes used for image acquisition and reconstruction, and SolidWorks and Zemax design files are publicly available on Duke Research Data Repository, doi:10.7924/r4474kt5f.

Submitted 9 July 2024
Accepted 7 April 2025
Published 9 May 2025
10.1126/sciadv.adr5912